This is the Author Accepted Manuscript of the following paper:
All-in-one supercapacitors with high performance enabled by Mn/Cu doped ZnO and MXene

Authors: Ameen Uddin Ammar, Feray Bakan-Misirlioglu, Mohamad Hasan Aleinawi, Giorgia Franzo, Guglielmo Guido Condorelli, Fatma Nur Tuzluca Yesilbag, Yasar Ozkan Yesilbag, Salvo Mirabella, Emre Erdem

Peer-reviewed and accepted for publication in:
Materials Research Bulletin, Volume 165, 2023, 112334

https://doi.org/10.1016/j.materresbull.2023.112334

All-in-One Supercapacitors with High Performance Enabled by Nanosized ZnO and MXene

Ameen Uddin Ammar[1], Feray Bakan-Misirlioglu[2], Mohamad Hasan Aleinawi[1]; , Giorgia Franzo[3], Guglielmo Guido Condorelli[4], Fatma Nur Tuzluca Yesilbag[5], Yasar Ozkan Yesilbag[5], Salvo Mirabella[4,6], Emre Erdem*[,1]

[1]Faculty of Engineering and Natural Sciences, Sabanci University, Tuzla 34956, Istanbul, Turkey
[2]Sabanci University Nanotechnology Research Centre (SUNUM), Sabanci University TR-34956 Istanbul, Turkey.
[3]IMM-CNR, via S. Sofia 64, 95123, Catania, Italy
[4]Dipartimento di Scienze Chimiche Università di Catania and INSTM UdR Catania 95125 Catania, Italy
[5]Department of Physics, Erzincan Binali Yıldırım University, Erzincan 24100, Turkey
[6]Dipartimento di Fisica e Astronomia "Ettore Majorana", Università di Catania, via S. Sofia 64, 95123, Catania, Italy

Corresponding: emre.erdem@sabanciuniv.edu

Abstract

Supercapacitors are gaining tremendous attention as energy storage devices for the benefits these devices can offer, like fast charge-discharge, high shelf life, and improved cyclic stability compared to other energy storage devices. Here in, we report the development of high-performance supercapacitor devices by using manganese-doped Zinc oxide nanowires (Mn-ZnO NWs) and Copper doped Zinc oxide nanoparticles (Cu-ZnO NPs) as one electrode and MXene as the second electrode material. The synthesis of all the electrode materials is reported along with the structural, electronic, optical, and electrochemical analysis. Transitional metal doped ZnO (TM-ZnO) have intrinsic and extrinsic defect signals, which were analyzed by Electron paramagnetic resonance spectroscopy (EPR) and photoluminescence spectroscopy (PL), the presence of these defects increases the overall synergy between the components of supercapacitor device which leads to enhanced performance of our supercapacitor. TM-ZnO samples when used in combination with MXene as a second electrode, increased the performance of supercapacitors even further as MXene offered high conductivity and high surface area. The electrochemical result of the assembled supercapacitor when measured by techniques like Cyclic voltammetry, impedance spectroscopy, and Galvanostatic charge-discharge showed some encouraging results to pursue this direction further. The highest performance value for a supercapacitor was obtained to be 1.67 Wh/kg energy density and a power density of 1495.5 W/kg.

1. Introduction

As the world has started shifting more towards clean and green energy resources, the demand for energy storage devices is increasing significantly [1]. Apart from batteries and conventional capacitors, supercapacitors are one new device, which is attaining great interest from researchers. Supercapacitor devices showed the potential to dominate the energy storage device market with their impressive properties like high power density, longer shelf life, fast charge and discharge, and cycle stability [2, 3]. The advantages that supercapacitors offer can easily bring them to commercial use but the lack of energy density values in supercapacitors compared to a battery is one of the primary hindrances in achieving this goal. Researchers are constantly looking for more ways of reaching high energy density values and in that search investigates new and innovative electrode material that can be used in supercapacitors which can increase the specific capacitance of the device which will eventually lead to high energy density values [4]. The selection of electrode material is of vital importance in supercapacitor devices. A good electrode material when coming in contact with other supercapacitor components tends to increase the overall synergy between the components, leading to the high performance of the device [5].

Different types of electrode materials are constantly been part of the investigation as they showed the potential of enhancing the performance of supercapacitor devices[6]. Transition metal oxides are among the popular choices to be used as electrode material. Metal oxides like NiO [7], MnO_2 [8], RuO_2 [9], and TiO_2 [10] have already been used in supercapacitors and have shown some positive results. In these metal oxides, ZnO is one of the most popular types of electrode material. ZnO is a highly defective semiconductor with naturally wide band energy at room temperature. ZnO offers other advantages like increased electrochemical activity, abundance in availability, environmental friendliness, etc., making ZnO a prevalent choice as electrode material [11-14]. The defective nature of ZnO serves as a considerable advantage in using ZnO as an electrode material. Defects in ZnO can be tailored to enhance further its performance as an electrode material [15]. The intrinsic defects in ZnO are usually Zinc vacancy, zinc interstitial, oxygen vacancy, and oxygen interstitial. These defects centers can be ionized and become paramagnetic, which is studied by EPR, a thorough discussion of the defects of ZnO is done in the author's previous work elsewhere for further understanding [16]. Sometimes to further enhance the material performance, ZnO is doped with other metal ions, and doping of ZnO improves the electrical and optical properties. For example, doping with metal ions develops a point defect in the ZnO lattice, which becomes very useful in the accumulation of charges and assists in forming the intrinsic defect. These intrinsic and extrinsic defects in lattice increase the electrochemical performance of the material. Different metal-doped ZnO had already been reported in the literature used in supercapacitor applications and showed promising results [17].

Recently, a new family of 2D materials referred to as MXenes has come into the limelight and has shown the significant potential of being an electrode material in energy storage devices. MXene base electrode provides exceptional electrical and electrochemical properties such as conductivity, hydrophilicity, and higher surface area. These properties make MXene an excellent electrode material to be used in supercapacitor devices as has already been tried in some previous work [18-20]. MXenes are the 2D materials synthesized by the etching of “A” layers from the layered carbides or carbonitrides commonly known as the MAX phases. They possess the structural formula $M_{n+1}AX_n$, where M is an early transition metal, A is usually III-A and IV-A group elements, X is carbon and/or nitrogen, and n= 1, 2, or 3. Selective etching is an essential condition for obtaining MXene. The most common method for synthesizing MXene is wet etching [21]. Thus, acidic solutions (HF or LiF + HCl) containing predominantly aqueous fluoride are used to selectively etch the "A" element layers from the MAX layered structures. In the etching with hydrofluoric acid (HF), various MXenes were synthesized from room temperature to 55 ^{o}C by controlling the reaction time and concentration. Experimental results showed that longer and more concentrated etching conditions are needed at larger atomic numbers of "M" [22]. Etching is a controllable kinetic process requiring different etch times for each MXene to be converted. Instead of HF, a mixture of lithium fluoride salt (LiF) and hydrochloric acid (HCl) can be used to synthesize MXene [23]. For example, HCl and LiF react to form HF that selectively etches atoms "A". However, recent studies obtained similar etching results using a mixture of HF and LiCl [24]. In other words, the presence of proton and fluoride ions in the medium is essential to obtain MXene with etching. Each MXene is generally synthesized with different qualities (defect concentration and surface chemistry) under various etching conditions [25]. The authors have published a comprehensive review showing the advantages of using MXene and ZnO as electrode materials [26].

Several studies previously revealed the superiority of MXene as electrode material in supercapacitors. Xia *et al*. reported high conductivity and a larger surface area which are key factors to supercapacitors performance, by synthesizing carbon-supported TiO_2 on $Ti_3C_2T_x$ MXene surface area. The supercapacitor device showed phenomenal performance where the maximum specific capacity of 92.0 $mAhcm^{-3}$ at 1 Ag^{-1} was reported and the maximum energy density of $1.04x10^{-2}$ $Wh.cm^{-3}$ at a power density of 0.22 $W.cm^{-3}$ [19]. Liu et al. achieved improved performance by combining reduced graphene oxide with MXene to attain 3D hybrid aerogels as supercapacitor material, the assembled supercapacitor showed the maximum specific capacitance of 345 Fg^{-1} at a current density of 1 Ag^{-1} [27]. Zhang et al. performed studies on improving the MXene component of the supercapacitor by forcing more -O termination, which in turn yielded a significant improvement in the supercapacitor performance. The electrode material when used in a supercapacitor showed a maximum capacitance value of 303 Fg^{-1} and excellent cyclic stability [28]. Kannan et al. worked on the development of ZnO-Fe-MXene nanocomposite which showed the promising result as an electrode material when used under a CO_2 atmosphere, the developed electrode material also provides interesting features for CO_2 reduction [29]. Wei et al. developed an MXene-MnO_2

electrode-based asymmetric supercapacitor and reported tremendous application prospects for these devices for next-generation energy storage devices. The performance of the developed supercapacitor showed excellent results, where the maximum specific capacitance reported was 20.5 Fg^{-1} at a current density of 1.5 at Ag^{-1} and the energy density for the device reported was 6.4 $Whkg^{-1}$ at 1107.7 Wkg^{-1} power density [30]. Li et al. reported $Ti_3C_2T_x$ anodes for asymmetric supercapacitors, with different combinations of carbon nanotube used and high performance of the device was reported. The maximum areal capacitance was reported at 2.26 F cm^{-2} and the areal energy density of 0.44 $mWh.cm^{-2}$ at 2.09 $mW.cm^{-2}$ power density [31].

In this work, high-performance next-generation supercapacitor devices were assembled using a combination of MXene as one electrode and Mn-doped zinc oxide nanowires (ZnO NW) & Cu-doped zinc oxide nanoparticles (ZnO NP) as another electrode. This study showed the synthesis route of all the electrode materials used and the characterization techniques to analyze these electrode materials. Electron paramagnetic spectroscopy (EPR) and photoluminescence spectroscopy (PL) are the two major characterization techniques for detecting defect centers due to their superior sensitivity and detection principle. This work summarizes the effect of different metal-doped ZnO on supercapacitor performance and also when used in combination with MXene as electrode material. This paper also talked about how different morphology of metal-doped ZnO can affect the supercapacitor performance. The electronic, optical, and electrochemical properties of the electrode material were reported, and the impact of different concentrations of metal ions on the performance of the supercapacitor was shown.

2. Sample Preparation

2.1 Synthesis of Mn-doped ZnO:

Mn-doped ZnO (ZnO: Mn) nanowires were synthesized using the typical hydrothermal route, by applying some modifications to the process. The precursor materials used were zinc nitrate hexahydrate (ZNH) ($Zn(NO_3)_2.6H_2O$) from Acros organics, hexamethylenetetramine (HMTA) ($C_6H_{12}N_4$) from Merk, manganese acetate tetrahydrate (MAT) ($C_4H_6MnO_4$) from Acros organics, and pure methanol (CH_3OH) from Sigma Aldrich.

Equimolar solution of 25 mM of ZNH and HMTA dissolved in de-ionized (DI) water and stirred with an RPM of 500 for 1 h at room temperature in a beaker. In a separate beaker, MAT is dissolved in methanol while continuously mixed until fully dissolved. The two solutions are then mixed and stirred at room temperature and 500 rpm for 10 min. The mixed solution is then placed in a commercial microwave oven and heated for 20 min at 160 W and 800 W microwave power output. The product, white powder is filtered and washed thrice with DI water, once with absolute alcohol to remove any impurities, and dried in the oven at 90 °C for 9 h. Finally, the dried powder is calcined at 300-500 °C for

2 h (depending on MAT mol%). The main control parameters for the synthesis process are MAT mol%, microwave oven power output, and calcination temperature.

2.2 Synthesis of Cu-doped ZnO:

The typical co-precipitation method was used to synthesize Cu-doped ZnO (Cu-ZnO) nanoparticles. The precursor materials used for the preparation were zinc nitrate hexahydrate (ZNH) ($Zn(NO_3)_2.6H_2O$) from Acros organics, copper nitrate (II) trihydrate (CNT) ($Cu(NO_3)2.3H_2O$), and sodium hydroxide pellets (NaOH) from Sigma Aldrich.

A solution of 3 M NaOH was prepared, dissolving NaOH pellets in DI water and stirring for 15 min at 500 rpm and room temperature until fully dissolved. This NaOH solution was used to control the pH value of the solution to the desired number. ZNH and CNT are dissolved in DI water (1, 2, and 5 wt %) in a separate beaker and stirred for 15 min at 500 rpm at room temperature until fully dissolved. The NaOH solution is added drop by drop in the mixture of ZnH and CNT to reach the pH of 14. As NaOH solution is added, foam and a blue precipitate can be noticed. Once the desired pH value is reached, the solution mixture is kept stirring at 500 rpm and room temperature for 30 minutes. Finally, the blue powder is filtered and washed thrice in DI water and absolute alcohol. The product powder is then dried at 80 °C for 9 h in the oven.

2.3 Synthesis of MXene

The $Ti_3C_2T_x$ MXene used in this study was synthesized from the Ti_3AlC_2 MAX phases by selective etching of Al atomic layers. In this method, 1 g of Ti_3AlC_2 powder (particle size <44 µm) was slowly added to a solution of 1.8 g of LiF in 20 mL of 9 M HCl acid and etched at 700 rpm for 24 h at 40 ^oC with the help of a magnetic stirrer. After etching, this mixture was centrifuged using de-ionized water at 3500 rpm until the pH value was ~6-7, and each cycle, the acidic supernatant was decanted. An ultrasonic sonicator was used for 30 minutes to delaminate $Ti_3C_2T_x$ MXene layers. Then, a vacuum filtration system with Celgard 3501 separator was used to obtain $Ti_3C_2T_x$ MXene in paper form, while the freeze-drying method was used to obtain $Ti_3C_2T_x$ Mxene in powder form.

3. Characterization

X-ray diffraction patterns were collected from a Bruker D2 phase diffractometer in the 2θ range from 10° to 90° using Cu Kα radiation (λ = 1.5405 Å). In this study, Raman measurements were performed with a high-resolution Raman spectrometer (Renishaw inVia, UK) with a 532 nm frequency-doubled Nd: YAG excitation source in combination with a 1200 lines/mm grating. The morphology of samples were observed by the aid of Scanning Electron Microscopy (SEM) (JEOL, JSM-6010LV) at 5 kV. Spectra were recorded with a PHI 5000 Versa Probe Instrument equipped with a monochromatic Al Kα X-ray source excited with a micro-focused electron beam. Analyses were carried out at 15 W on 150 □m area with a photo-electron take-off angle of 45°. X-band (9.63 GHz) electron paramagnetic resonance (EPR) measurements were

conducted on a Bruker EMX Nano at room temperature at 10 mW microwave power. The photoluminescence (PL) of Mn: ZnO was recorded using a spectrofluorometer FS5 with a 320 nm excitation wavelength with a Xe lamp used as a light source, 5 nm excitation slit distance, and 10 nm emission slit distance. The MXene PL spectra were measured on the same instrument with 300nm as excitation wavelength. The Cu:ZnO sample PL measurements were performed by pumping with the 325 nm (3.82 eV) line of a He–Cd laser chopped through an acousto-optic modulator at a frequency of 55 Hz and a fixed power of 1.5 mW. The PL signal was examined using a single grating monochromator, detected with a Hamamatsu visible photomultiplier, and recorded with a lock-in amplifier using the acousto-optic modulator frequency as a reference.

Electrochemical measurements were performed using a Biologic VMP 300 multipotentiostat with the standard two-electrode technique. The electrolyte used for all the test samples was 6M KOH with glass fiber as a separator.
The performance of the SCs and electrochemical performance of the electrode material were tested using Cyclic Voltammetry (CV), Galvanostatic cycling with Potential Limitation technique (GCPL), Electrochemical Impedance Spectroscopy (EIS), and voltage holding experiments. CV curves were recorded in a voltage range of 0 to +1 V at scan rate of 100 mVs^{-1} . EIS results were completed by applying a sinusoidal signal of 10 mV from a 10 mHz to 1 MHz frequency range. GCPL was done within a voltage window from -1 to +1 V at a specific current density of 0.10 A/g , 0.15 A/g, 0.20 A/g, 0.30 A/g and 0.50 A/g.

4. Results & Discussion

4.1 XRD Analysis

The structural analysis of the sample was done by XRD analysis. Figure 1 shows the undoped ZnO NWs and doped samples with various Mn concentrations all exhibit a typical wurtzite structure of ZnO corresponding to peaks of (100), (002), (101), (102), (110), and (103). These results were expected since Mn^{+2} replaces Zn^{+2} without altering the wurtzite structure due to having a similar ionic radius [32]. The graphs also show that increasing Mn concentrations shift the peaks towards lower 2θ values due to the slight difference between Mn and Zn ionic radius, which are 0.68 Å and 0.75 Å, respectively. Figure 2 shows the XRD for the Cu-doped sample, like the Mn-doped sample. we observed peaks for the typical wurtzite structure of ZnO. It shows that the Cu dopant did not affect the ZnO lattice due to a similar ionic radius, Cu^{+2} has a radius of 0.73 Å, and Zn^{+2} has a 0.75 Å ionic radius. Although for Mn-doped ZnO NWs for 800 W samples and Cu-doped samples, we observed that as we increased the amount of dopant concentration, an additional peak is observed for the Mn sample at (400) and Cu-doped sample at (111). The formation of a new peak around 38° can be noticed at (111), which is associated with a CuO phase [33], and for the Mn sample at around 2θ°= 43.5° corresponding to $ZnMnO_3$ impurity as explained previously in the literature [34].

Figure 3 shows the XRD pattern for the Ti_3AlC_2 (MAX) and $Ti_3C_2T_x$ (MXene). MAX phase has its primary peak at 9.1° and 19.6° which corresponds to the (002) and (004) respectively [35, 36]. These peaks in MXene shift towards a lower angle. This can be attributed to the increase in interplanar spacing of MXene due to the etching of aluminum and the loss of the crystalline nature of the MAX powder [37]. The MAX phase peak at around 38°, which corresponds to the (104) plane belongs to aluminum, and almost the removal of this peak from MXene shows the successful etching of the aluminum layer.

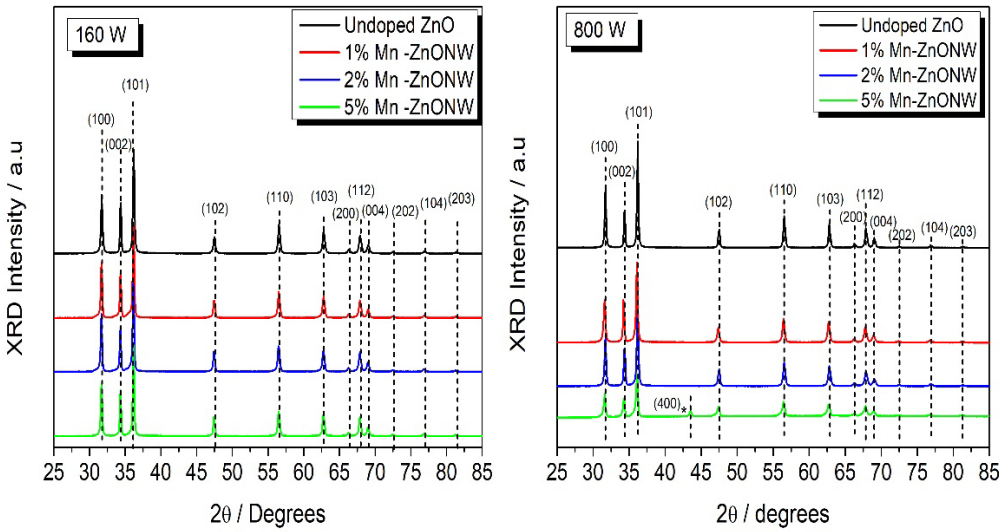

Figure 1: XRD pattern of Mn-doped ZnO NW at 1, 2 and 5 % doping concentration synthesized at 160 W (left) and 800 W (Right)

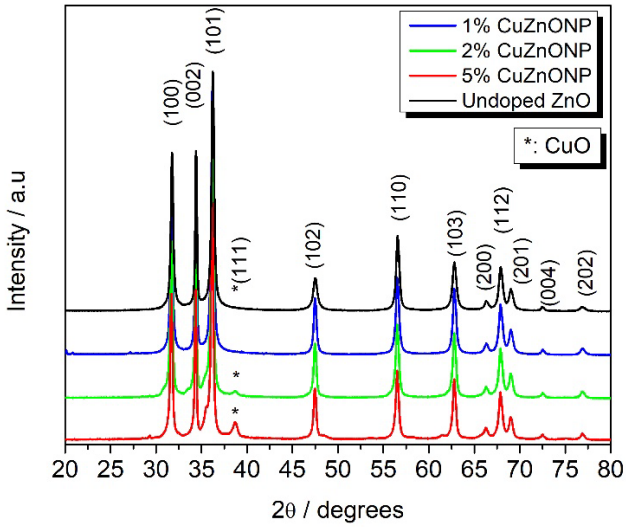

Figure 2: XRD pattern of Cu doped ZnO NW at 1, 2, and 5 % doping concentration

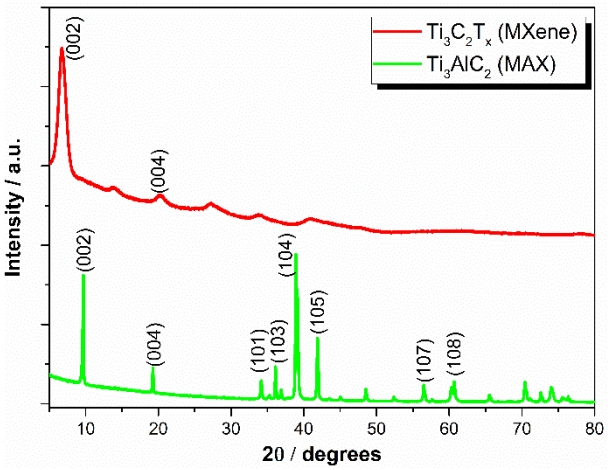

Figure 3: XRD pattern for Ti_3AlC_2 (MAX) and $Ti_3C_2T_x$ (MXene).

4.2 Morphological Analysis

The morphology of the synthesized metal-doped ZnO was studied by SEM. Figure 4 (a) and 4 (b) clearly show how different synthesis route gives different morphology for the metal-doped ZnO. Mn-doped ZnO clearly showed rod-like morphology with an average length of 600 nm and a maximum diameter of 90 nm. A detailed analysis of Mn-doped ZnO showed a nanowire morphology is available in our previous work [38]. Cu-doped ZnO showed disk-like morphology with rough edges and surfaces and had a diameter of approximately 400 nm and a thickness of about 40 nm.

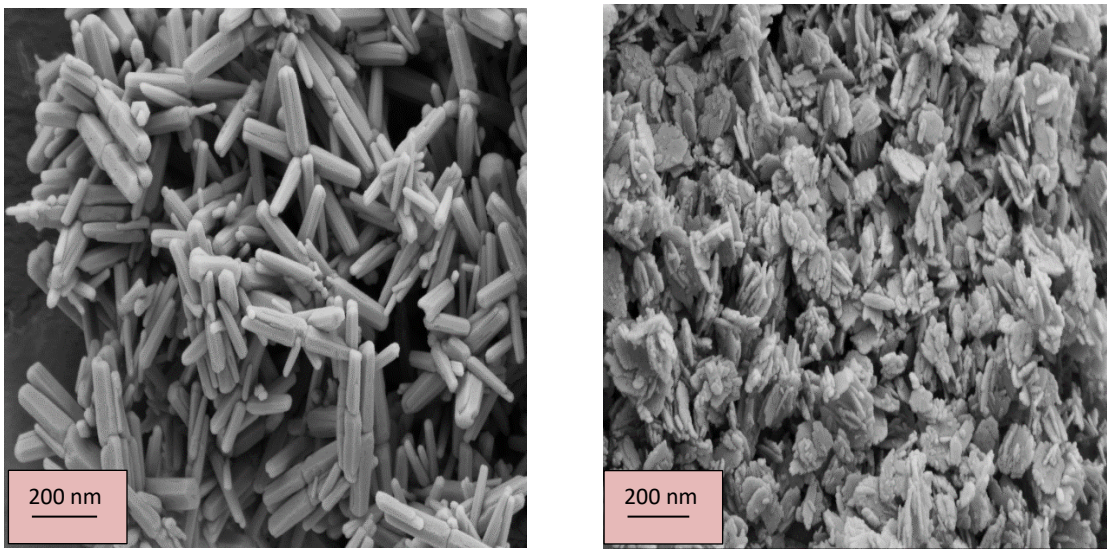

a) b)

Figure 4: SEM images of (a) Mn-doped ZnO NW and (b) Cu-doped ZnO NP

4.3 Raman Spectroscopy Results

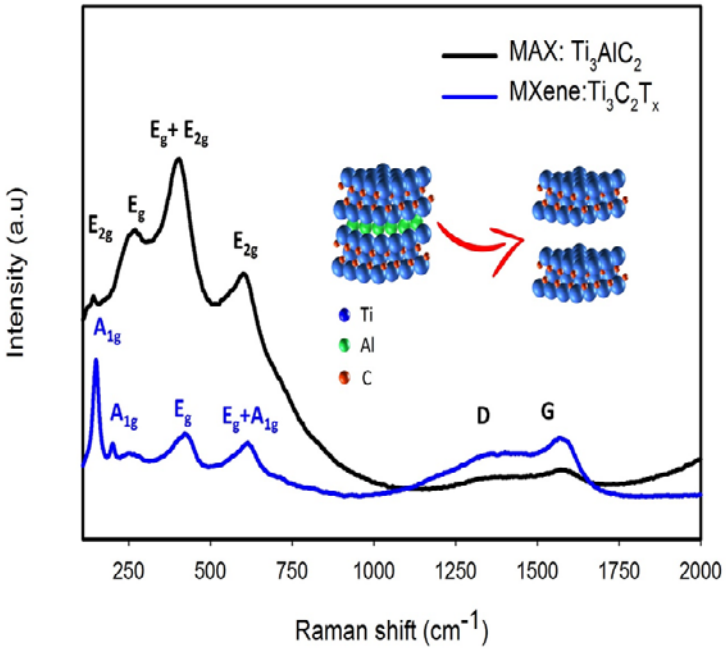

Figure 5: Raman Spectra of MAX phase (Ti_3AlC_2) and MXene ($Ti_3C_2T_x$)

Raman spectroscopy has greatly contributed to the understanding of not only the phonon spectra and structural features of nearly all known 2D materials, but also their mechanical, thermal, and electronic properties. Therefore, Raman spectroscopy emerges as an important analysis method for the characterization of new 2D materials such as MXenes. Figure 5 shows the Raman spectra of the Ti_3AlC_2 starting material in the MAX phase and the obtained $Ti_3C_2T_x$ Mxene. It is known that Ti_3AlC_2 (312 phase) belongs to the P63 /mmc space group, and among 33 optical modes, seven Raman-active first-order vibrations ($2A_{1g} + 2E_{1g} + 3E_{2g}$) can be present in this system. However, up to date, only six Raman-active modes have been reported [39]. In the MAX spectrum (Figure 5), the weak and strong peaks observed around 141, 269, and 601 cm^{-1} were labeled as E_{2g}, A_{1g}, and E_{2g} respectively. These peaks are the key features of Ti_3AlC_2 and match well with those reported in the literature, attributed to shear and longitudinal oscillations of Ti and the Al atoms [39-41]. The weak peak at 141 cm^{-1} is a shear vibration involving the Al and Ti atomic planes. The peak observed at 270 cm^{-1} is likely due to the shear vibrations of the Al atomic planes in addition to the antiparallel shift of adjacent Ti atomic planes [42]. The broad and weak D- and G-bands, which may originate from the sp^2 regions of possible free carbons in the samples, were detected around 1350 cm^{-1} and 1570 cm^{-1} in the spectrum, respectively. While the G-band peak is associated with the stretching of the C-C bond in all sp^2 carbon systems including both rings and chains, the D peak depends on sp^2 fraction and order and appears only if the sp^2 is in disordered rings [43, 44].

In the case of Ti_3C_2, vibrations of this structure can be described as $4E_g + 2A_{1g} + 4E_u + 2A_{2u}$. Among these vibrations, only E_g (in-plane vibrations of Ti and C atoms) and A_{1g}

(out-of-plane vibration of Ti and C atoms) are Raman-active. However, it should be kept in mind that lattice vibrations can be affected by the presence of active groups (T_x) on the surface, causing peak shifts and alterations in the spectra. In the MXene spectrum, the peaks at 150 cm^{-1} and 199 cm^{-1} can be assigned to in-plane A_{1g} (Ti, O, and C) modes, while the peak at 424 cm^{-1} was assigned to out-of-plane E_g modes of surface groups attached to Ti atoms [41]. The peak at 614 cm^{-1} can be attributed to both in-plane and out-of-plane carbon vibrations. Similar to the MAX phase, the broad D and G bands at around 1350 and 1570 cm^{-1} were attributed to the presence of amorphous carbon in the MXene spectrum.

4.4 XPS Analysis

To obtain further information on the surface chemistry of the MXene, XPS analysis is performed and the result is shown in figure 6. The graphs showed obvious signals from Ti, C, O, and F elements. High-resolution XPS spectra in the C 1s region (Figure 6b) of the MXene powder showed four main peaks at 281.8, 285.0, 286.5 and 288.3 eV which originate from Ti-C, C-C, C-O and C=O/COO-, respectively . The presence of C-O can be attributed to TiO_2 and carbon atom networks which may arise due to the oxidation of MXene [45]. Figure 6c shows the high-resolution spectra of the Ti 2p region which shows peaks when deconvoluted into components corresponding to Ti-C, $Ti(_{II})$, $Ti(_{III})$ $Ti(_{IV})$, and Ti-F. The Ti-C signal is considered to be coming from Ti atoms in the interior of the MXene layers [46-48]. The Ti signal from different oxidation states like $Ti(_{II})$, $Ti(_{III})$ $Ti(_{IV})$ arises from the formation of mixed oxides/flourides (TiO_xF_y) and carbon oxides (TiC_xO_y) showing that the termination of the MXene surface is not homogenous [45]. Figure 6 (d) shows the high-resolution spectra of O 1s regions which shows the presence of Ti-O, Ti-OH, C-O, and C-OH. Figure 6 (e) clearly shows Ti-F which confirms the presence of F groups were present due to etchant.

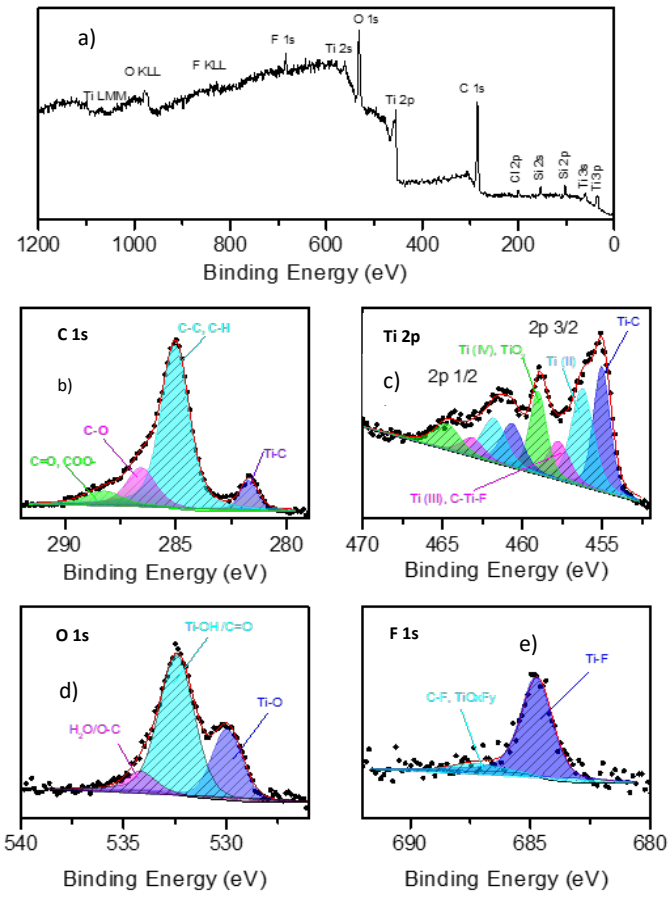

Figure 6: XPS spectra of MXene($Ti_3C_2T_x$) powder: (a) survey, (b–e) high resolution spectra of C 1s, Ti 2p, O 1s, and F 1s regions, respectively

4.5 EPR Spectroscopy Results

The EPR spectroscopy of Mn-doped ZnO NW and Cu-doped ZnO NP are shown in Figures 7 and 8. EPR spectroscopy is a very powerful tool for identifying the paramagnetic defect centers. These defect centers play a vital role in improving the electrode material's performance by increasing the electrochemical activities (active sites). Figure 7 shows the EPR spectra of the Mn-doped ZnO NW samples manufactured at 160 W and 800 W. Both the samples reveal the g=1.96 peak which is attributed to the core defects. However, the presence of surface defects at g~ 2.02 which is observed in some of the author's previous work might be fainted or suppressed by the high intensity of core defects. The complete information on the core-shell model and EPR spectra of undoped ZnO can be found in previous works [16, 49]. The intensity of the 160W sample appears higher than the 800W sample, while the 800W sample show more broadening compared to the 160W sample. Figures 6 also show the EPR spectra of Mn-doped ZnO NW samples prepared with 160W and 800W microwave power and using three different doping concentrations: 1, 2, and 5 mol %. EPR spectra of Mn-doped samples showed typical sextet hyperfine lines of Mn^{+2} which represent the successful incorporation of Mn^{+2} ions in the ZnO lattice. The sextet EPR signal due to the Mn^{+2} ions showed dominance on the intrinsic defects as the core signal at g=1.96 disappears even at 1 % doping

concentration. The trend of increase in EPR intensity and broadening of the peaks as the doping concentration increases can be seen in both 160 W and 800 W samples. It can be attributed to the increased Mn^{+2} - Mn^{+2} exchange and spin-lattice interactions with increased doping concentration. A detailed explanation of the EPR spectra of Mn-doped samples can be found in our previous work for a better understanding [38].

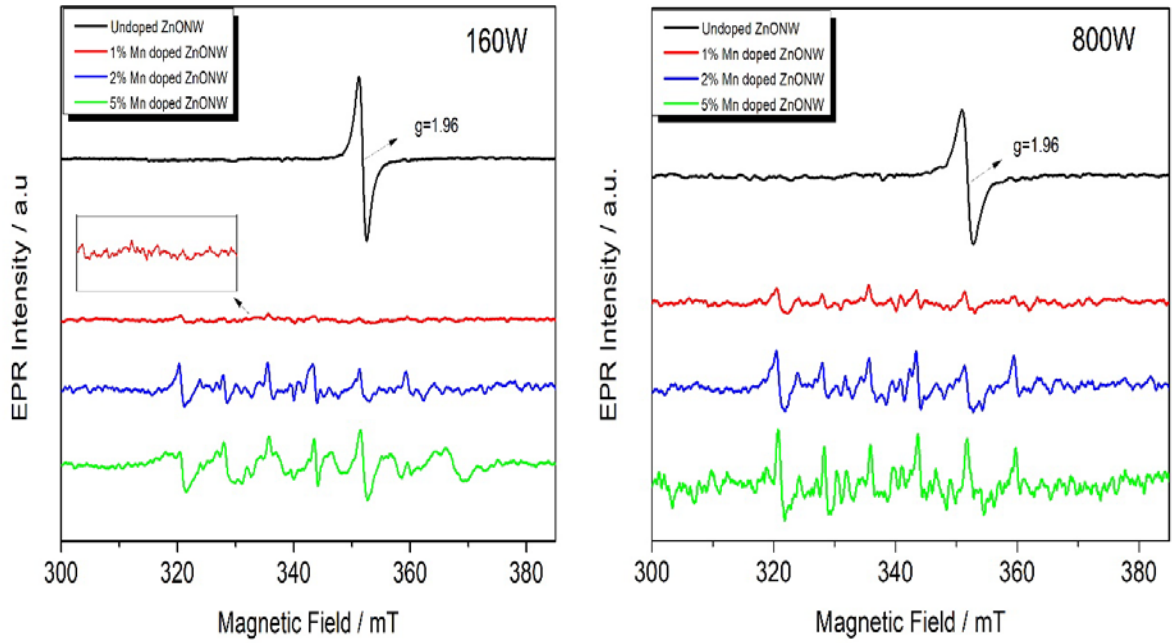

Figure 7: EPR spectra of Mn-doped ZnONW at 1, 2, and 5 % doping concentration synthesized at 160W(left) and 800W (Right)

Figure 8 present the X-band EPR spectra of Cu-doped ZnO NP at three different concentrations of 1, 2, and 5 mol%. The EPR spectra show the characteristic Cu^{+2} EPR signals with an axial g-tensor and a four-line hyperfine coupling pattern due to the Cu nuclear spin 3/2. The graphs show that as the doping concentration increases, the EPR signal becomes more complex in the high field region, and a new resonance appears. Although the external defect of Cu^{+2} ions is dominant in spectra, the core and surface signal form ZnO at g=1.96 and g ~2 are slightly visible due to suppressed intensity of external defects

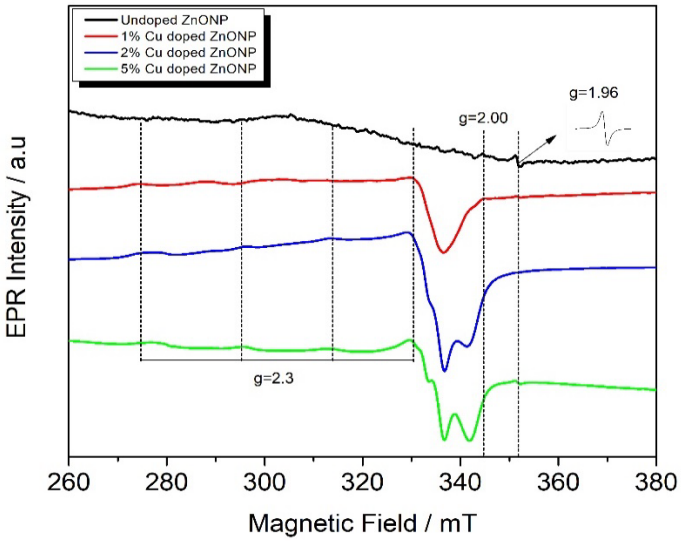

Figure 8: EPR Spectra of Cu doped ZnONP at 1, 2, and 5 % doping concentration

4.6 Photoluminescent Spectroscopy Results

Figure 9 and figure 10 showed the effect of Mn and Cu doping on the optical properties of the ZnO. The PL spectra present here showed intrinsic and extrinsic defects induce emissions in the visible light regions. Figure 9 shows the effect of increasing Mn concentration on the ZnO lattice. Compared to undoped ZnO as we increase the doping concentration, we observed a flattening of the PL emission signal. It represents the intrinsic defects that are suppressed by the dopant addition, indicating that the Mn ions have incorporated the ZnO lattice. A detailed description of PL spectra of Mn-doped samples can be found in previous work [38].

Figure 10 shows the PL spectra of Cu-doped ZnONP samples and the pattern is almost similar to Mn-doped samples. We observe that increasing the Cu ion concentration suppresses the emission signal from the intrinsic defects of the ZnO lattice and as the doping concentration of Cu ions increased the intensity of the PL signal decreased at a wavelength known as green luminescence indicating that Cu ions are incorporating in the lattice taking up zinc vacancies or interstitials in short extrinsic defects starts dominating over the intrinsic defects. Figure 11 shows the PL emission spectra of MXene when excited by 300 nm. The spectra showed emissions that peak at ~ 550 nm and this emission signal varied according to the excitation signal which represents that this result is in line with the previously reported results. The small image in the spectra showed the near-band emission of MXene when excited at 300 nm. The PL analysis of MXene showed that there are defect centers in MXene that become the reason for the emission signals but these defects are not paramagnetic as they were not detected in EPR. The defects signal for MXene like other 2D carbons are controversially discussed and generally, there are two reasons: size effect and surface defects [50, 51].

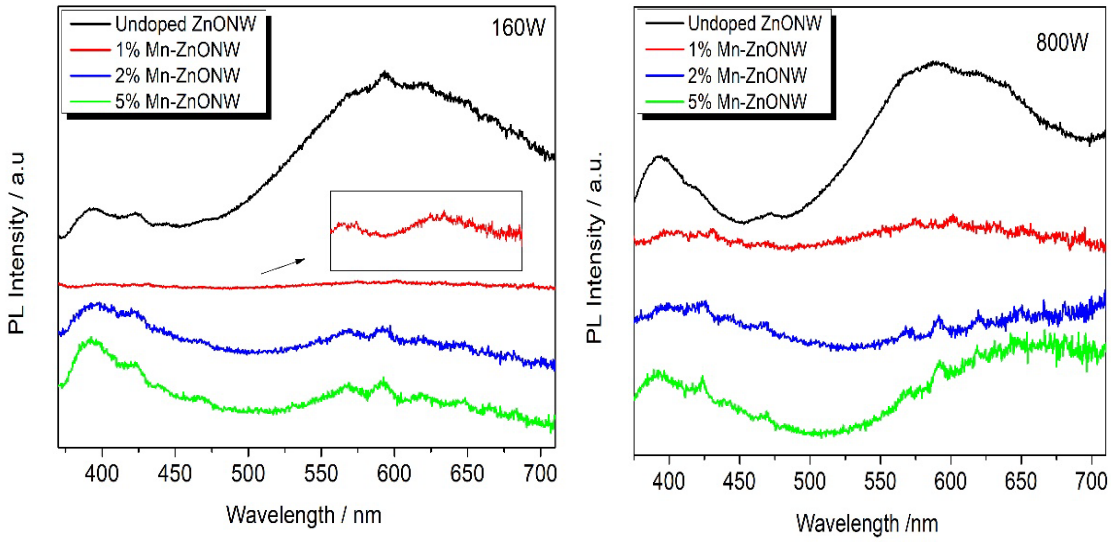

Figure 9: PL spectra of Mn-doped ZnONW at 1, 2, and 5 % doping concentration synthesized at 160 W(left) and 800 W (Right)

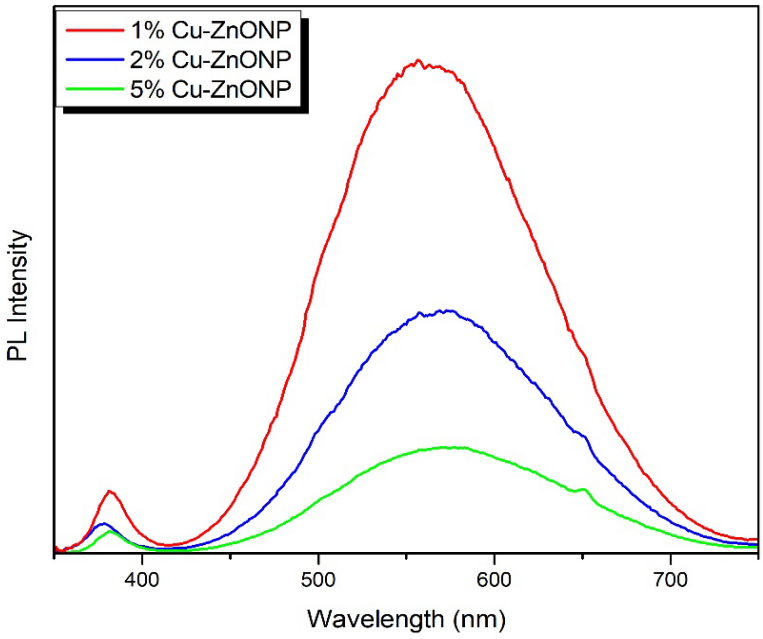

Figure 10: PL Spectra of Cu doped ZnONP at 1, 2, and 5 % doping concentration

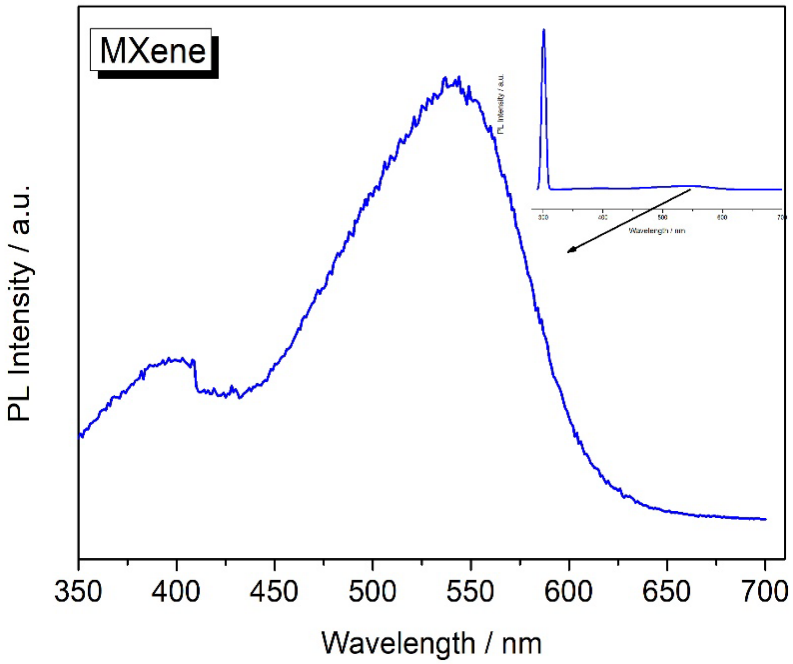

Figure 11: PL emission spectra of MXene excited at 300 nm.

4.6 Electrochemical Impedance Spectroscopy Results:

The electrochemical data are presented and compared based on dopant concentration. Similar dopant concentration data are shown together. Tables 1, 2, and 3 show the developed supercapacitor design and how they are compared. Apart from the design shown in the table, an MXene-based symmetrical supercapacitor is also prepared and tested to compare with other results.

Table 1: 1% doped ZnO-based supercapacitor design

Electrode 1	**Electrode 2**	**Electrolyte**	**Separator**	**Type**
1% Mn-doped ZnO NW 160W	MXene	6M KOH	Glass fiber	Asymmetrical
1% Mn-doped ZnO NW 800W	MXene	6M KOH	Glass fiber	Asymmetrical
1% Cu-doped ZnO NP 1	MXene	6M KOH	Glass fiber	Asymmetrical

Table 2: 2% doped ZnO-based supercapacitor design

Electrode 1	Electrode 2	Electrolyte	Separator	Type
2% Mn-doped ZnONW 160W	MXene	6M KOH	Glass fiber	Asymmetrical
2% Mn-doped ZnONW 800W	MXene	6M KOH	Glass fiber	Asymmetrical
2% Cu-doped ZnONP 1	MXene	6M KOH	Glass fiber	Asymmetrical

Table 3: 5% doped ZnO-based supercapacitor design

Electrode 1	Electrode 2	Electrolyte	Separator	Type
5% Mn-doped ZnO NW 160W	MXene	6M KOH	Glass fiber	Asymmetrical
5% Mn-doped ZnO NW 800W	MXene	6M KOH	Glass fiber	Asymmetrical
5% Cu-doped ZnO NP 1	MXene	6M KOH	Glass fiber	Asymmetrical

Figure 12 shows the CV curve of all the supercapacitor designs measured at a 100 mV/s scan rate. The graph shows the second cycle of the design except for the MXene symmetric figure 12 (d) which shows all 11 cycles, the shape for all of the designs appeared to be conical-tapered deviating slightly from the rectangular shape or else called quasi-rectangular. This shows for all the designs, the charge storage is due to the contribution of both electric double-layer capacitance (EDLC) and pseudo-capacitance (although no redox peaks are observed). The shape of the curve indicated good capacitive behavior of the supercapacitor and a fast charge-discharge process. The nanowires morphology, in general, showed a higher current value than the nanoparticles' morphology as can be seen in each of the dopant concentration graphs (Figure 12(a-c)). However, the 800W Mn-doped sample showed a high current value at each dopant concentration. The reason can be based primarily on the surface area of the electrode material. The high surface area provides more sites for the electrochemical reaction. It has been shown that nanowire morphology proves to be an excellent option for electrochemical reactions to take place. Nanowires as electrode materials provide increased electrochemical active sites for the redox reaction to take place. The nanowire structure increases the wettable surface area and improves the conductivity due to the 1-D structure of the nanowire [52, 53]. It also shortens the transportation pathway length and accelerates the faradic reaction. The highest value from the 800W Mn-doped sample can be attributed to the higher surface area of the 800W sample, the sample synthesized at 800W is denser and has a higher diameter value which results in more electrochemical sites for reactions to take place [53]. Figure 12 (d) shows the CV curve of the MXene symmetric supercapacitor design with all its 11 cycles presented. The curve shows the superior performance of this device compared to any other design, as this supercapacitor shows a higher current value of all cycles compared to any other supercapacitor design.

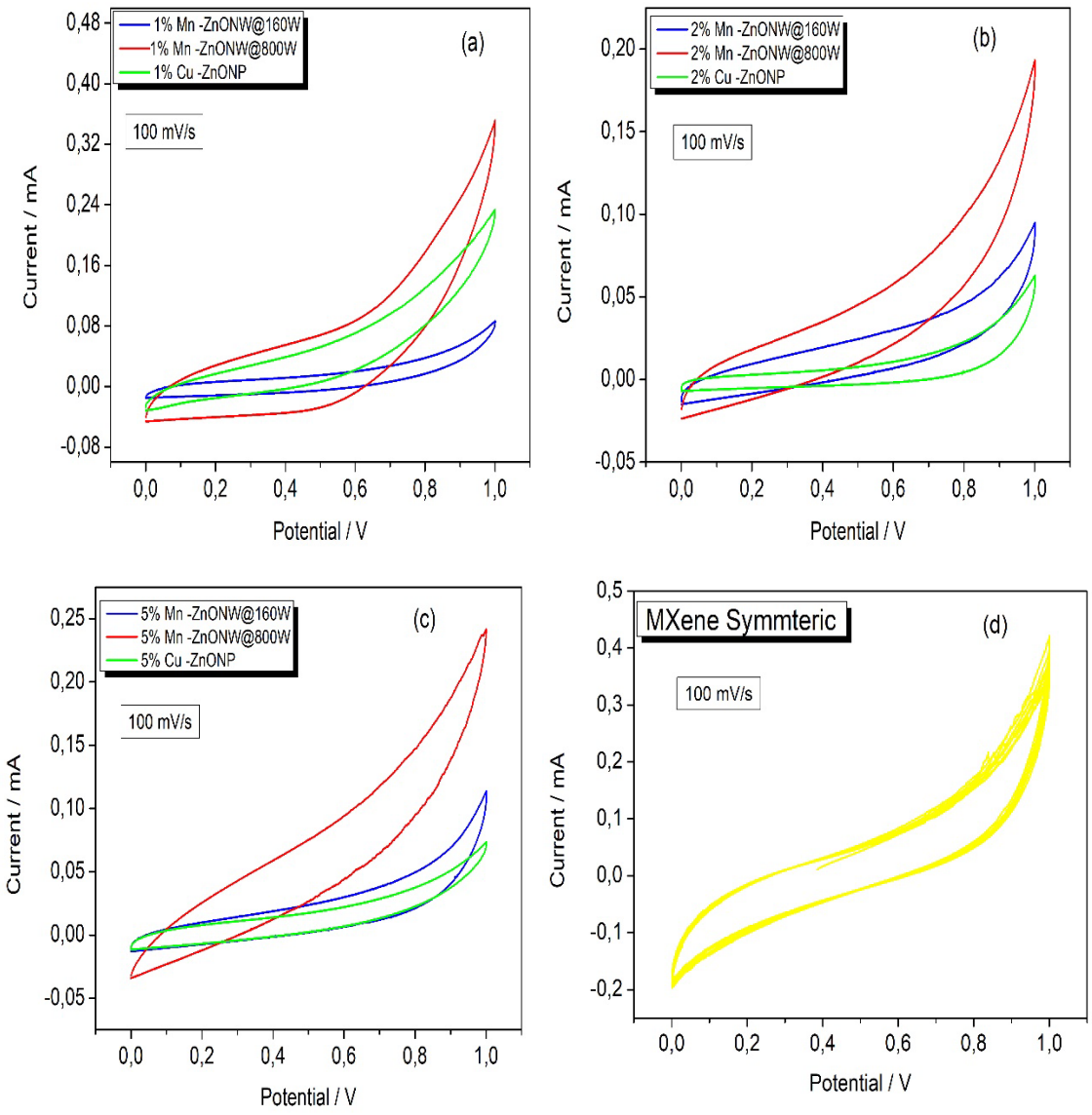

Figure 12: Cyclic Voltammetry scans supercapacitor designs: a) 1% doped samples, b) 2% doped samples, c) 5% doped samples, and d) MXene symmetric

Figure 13 shows the Nyquist plot for all the supercapacitor designs to show the electrochemical performance of the system. No semi-circle observed in the high-frequency region for any of the graphs indicates fast ion diffusion with no or negligible interfacial charge transfer resistances of the measuring electrodes. The MXene symmetric supercapacitor compares to all other designs shows the lowest value of impedance, which suggests better performance which is similar to the CV result. The Mn-doped sample of 800 W power in the Nyquist plot also in all dopant concentration values showed lower values of impedance in the high-frequency region compared to other asymmetrical designs, although at lower frequency regions we observed different trends in all the graphs. The Cu-doped sample generally showed a lower impedance

value than their counterparts in other concentration values. Figure 14 showed the equivalent circuit fitting of Nyquist plot data for all the doped ZnO samples. The x-intercept in Nyquist plots at high frequency represents the equivalent series resistance (R_S) which corresponds to the resistance of the electrolyte, the contact resistance of the interface between the current collector and the electrode and it also showed the resistance of the active material. Table 4 shows the Rs values of all the supercapacitor designs. The nanowires samples show lower values of contact resistance and 2% Mn-doped samples at 800 W recorded the lowest value of contact resistance which also has a steeper Warburg slope indicating the increased charge transfer and fast ion diffusion. The constant phase element (Q) present in all the equivalent circuits is to represent the deviation from the ideal capacitance and diffusion behavior due to the non-homogeneity of the surface at the electrode-electrolyte interface. Figure 15 shows the galvanostatic comparison of all the supercapacitor designs at a current density of 0.10 A/g. 800 W Mn doped sample shows the highest values of specific discharge capacities for 2% and 5% samples. In contrast, the Cu-doped samples show the highest values for the 1% sample. The trend for the graphs shows that as we increase the doping concentration, the value of specific capacity increase for the sample. Figure 16 shows the specific capacitance value at a different current density value, the pattern is similar to that of figure 7, 800 W Mn doped sample showed a high capacitance value for 2% and 5% doping concentration while Cu doped dominate the 1% sample.

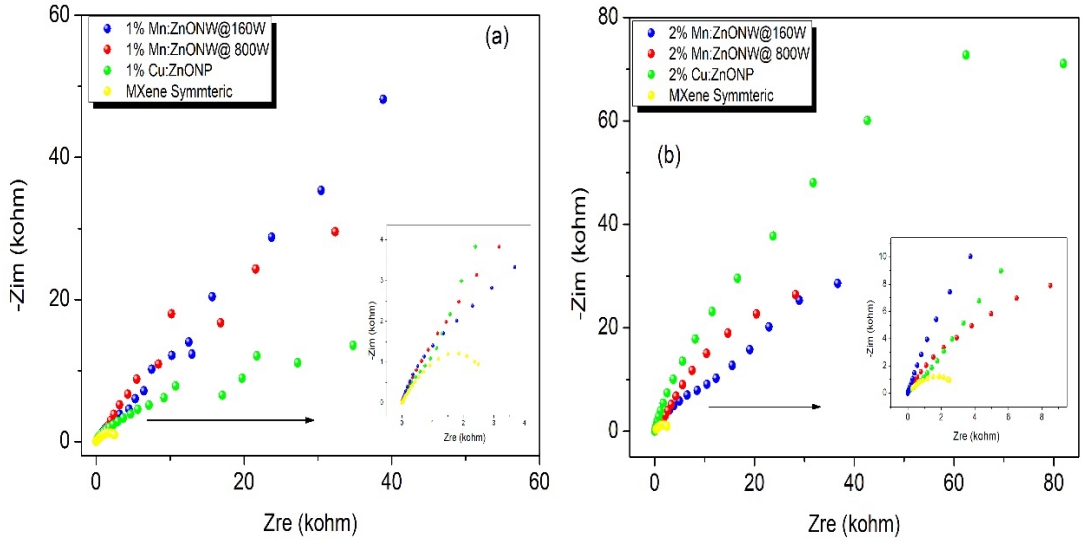

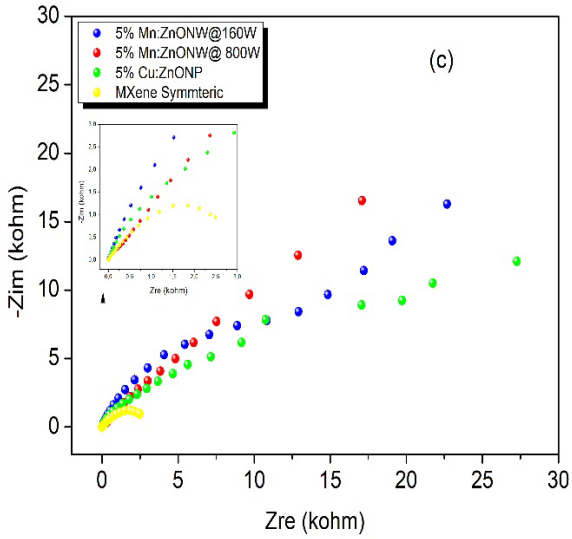

Figure 13: Electrochemical Impedance spectra (Nyquist plot) of Supercapacitor designs: a) 1% doped samples b) 2% doped samples and c) 5% doped samples

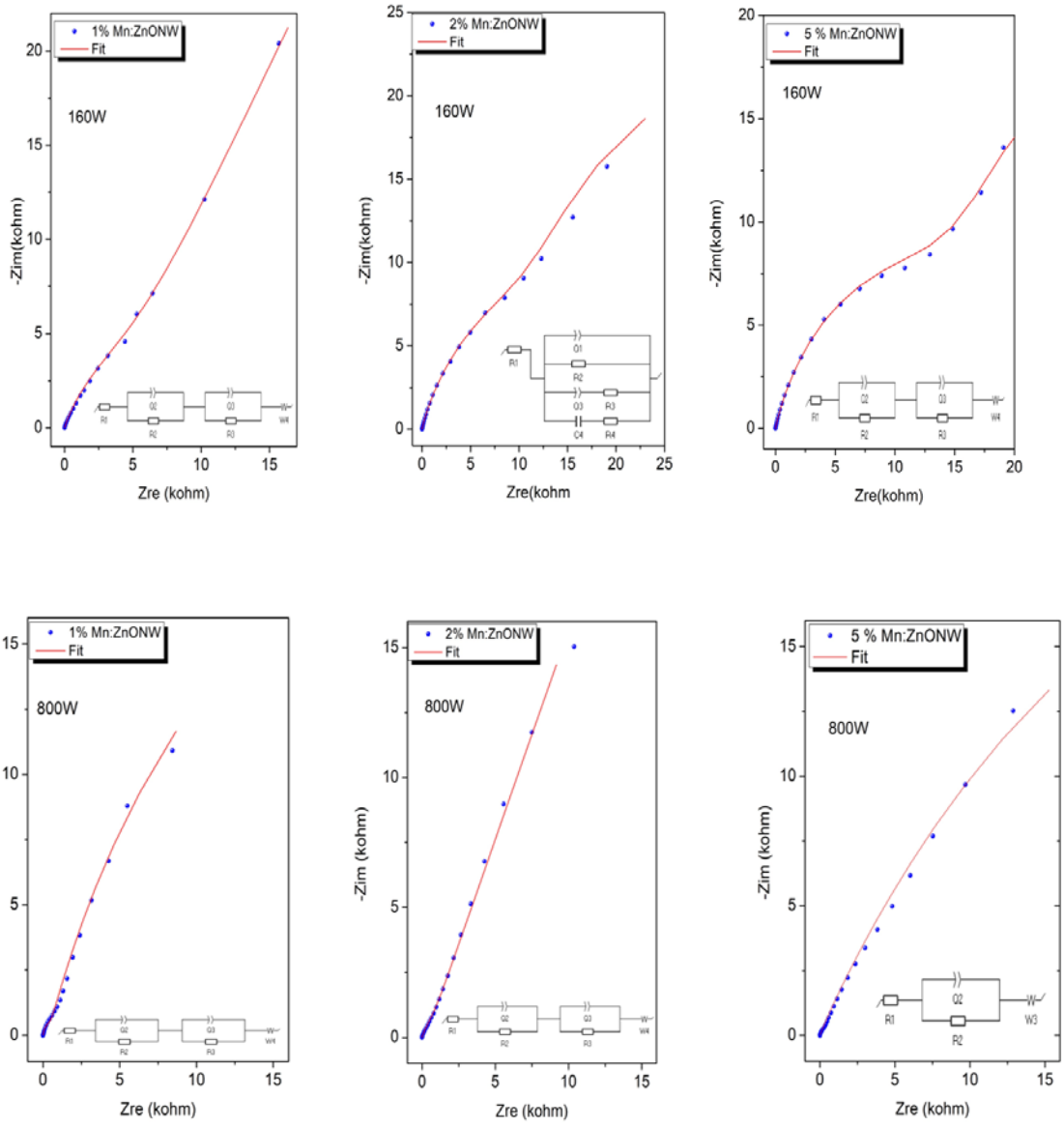

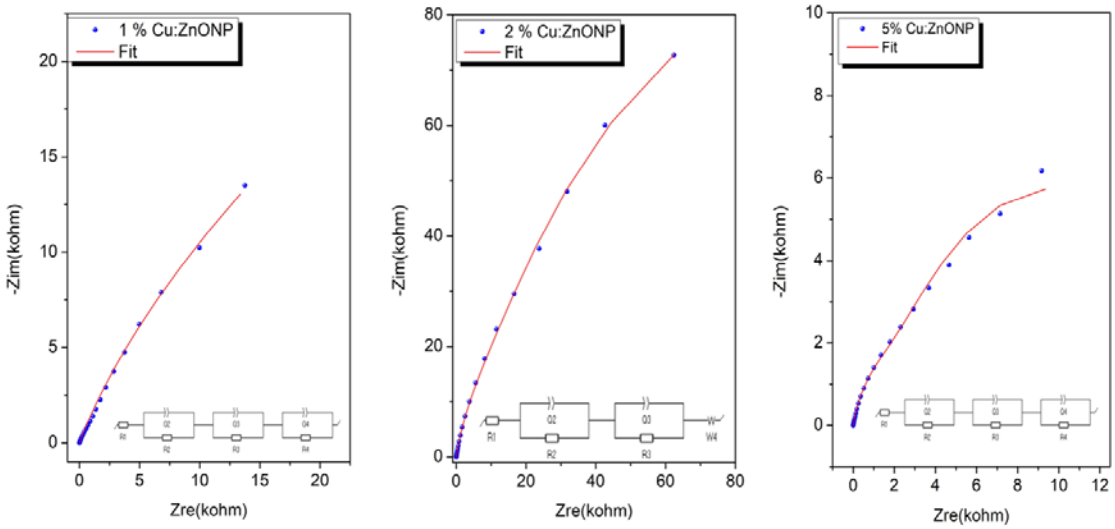

Figure 14: Equivalent circuit used to fit the Nyquist plot experimental data

Table 4: Equivalent Resistance value (Rs) of the assembled supercapacitor

	Rs (Ω)
1% Mn-doped ZnO NW 160 W	0.923
1% Mn-doped ZnO NW 800 W	0.7212
1% Cu-doped ZnO NP 1	1.546
2% Mn-doped ZnONW 160 W	0.3204
2% Mn-doped ZnONW 800 W	0.220
2% Cu-doped ZnONP 1	0.458
5% Mn-doped ZnO NW 160 W	0.533
5% Mn-doped ZnO NW 800 W	0.452
5% Cu-doped ZnO NP 1	1.093

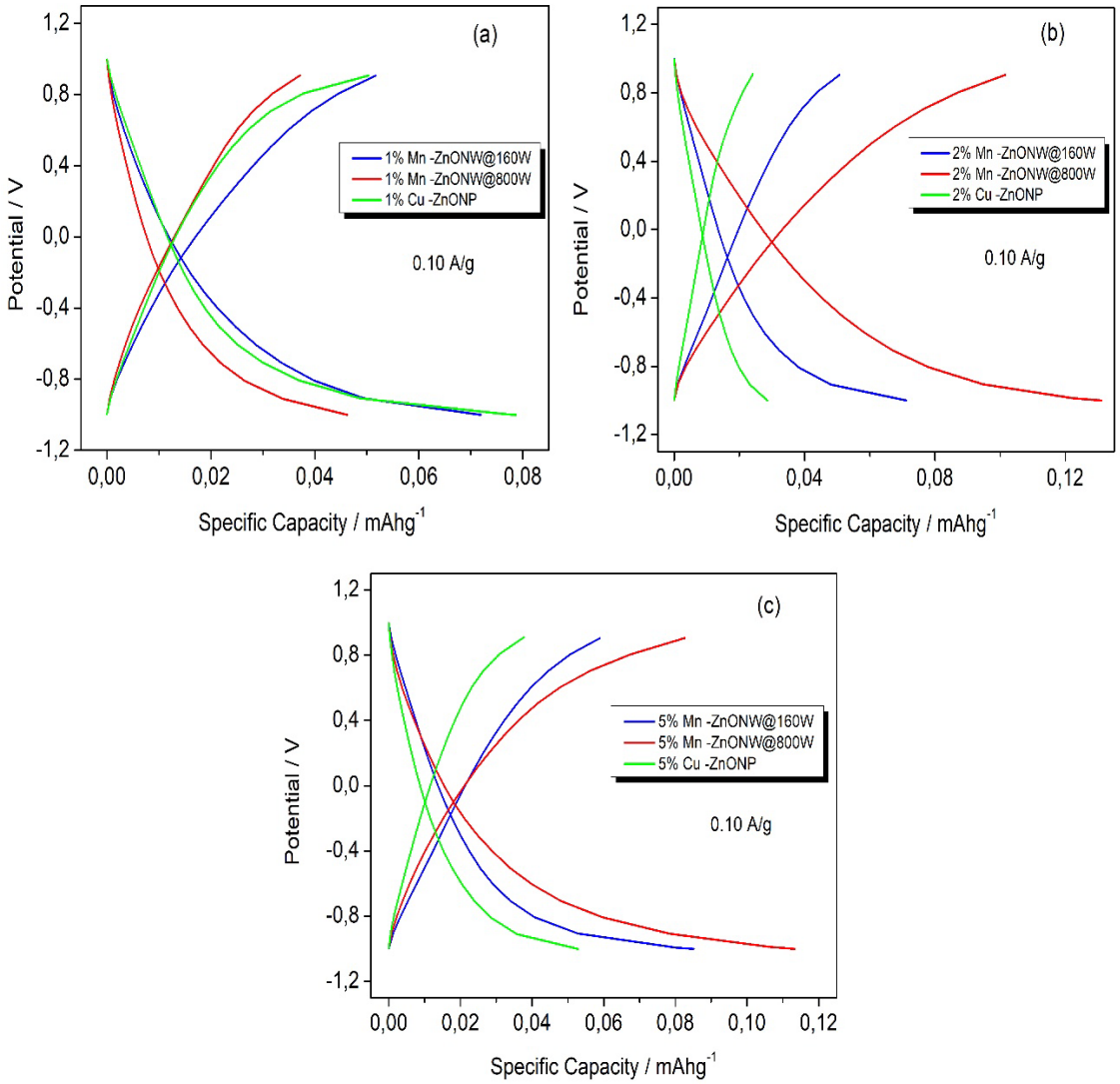

Figure 15: Galvanostatic charge-discharge curves of supercapacitor designs at 0.10 A/g current density: a) 1% doped samples, b) 2% doped samples, and c) 5% doped samples

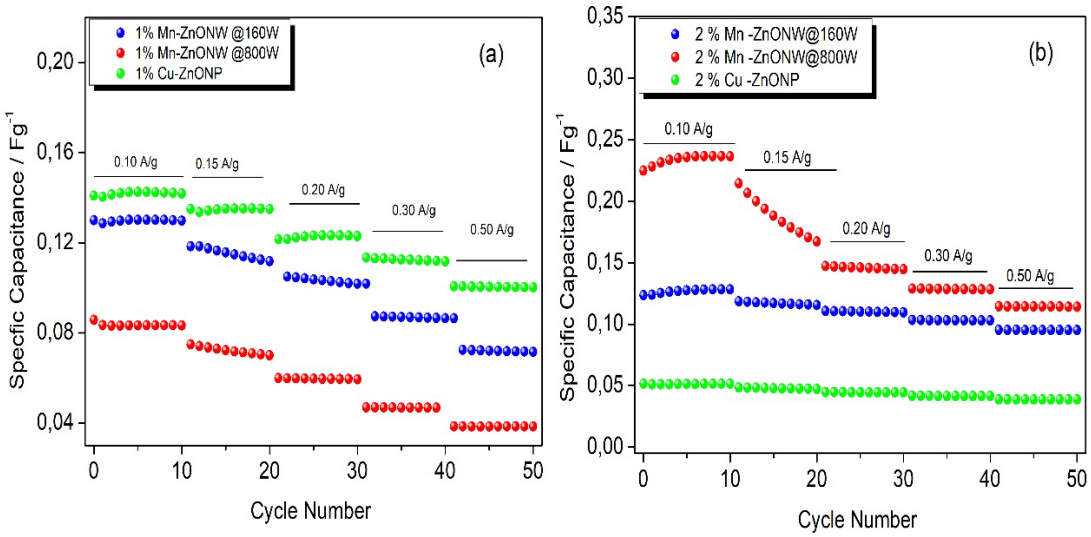

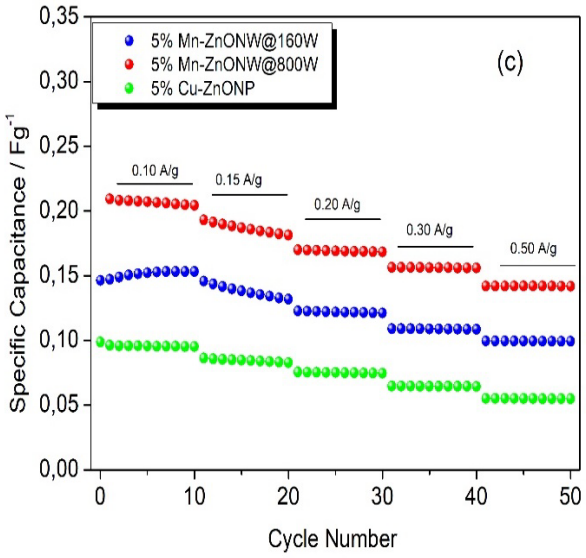

Figure 16: Cyclic performance of electrodes upon charging and discharging at different current densities: a) 1% doped samples b) 2% doped samples and c) 5% doped samples

The Ragone plot is a standard performance measuring criteria for energy storage devices where the energy density and the power density values are plotted for the devices. The energy density and power density of the developed supercapacitors were measured from the Galvanostatic charge-discharge data at a current density of 0.15 A/g using the following equations.

$$\mathrm{Csp} = \frac{\mathrm{Is}\,\Delta\mathrm{T}}{\mathrm{m}\Delta\mathrm{V}} \qquad (1)$$

$$\mathrm{Eg} = 1/2\,\frac{\mathrm{Csp}(\Delta\mathrm{V})^2}{3.6} \qquad (2)$$

$$\mathrm{Pg} = \frac{\mathrm{Eg}}{\Delta\mathrm{T}}3600 \qquad (3)$$

Where C_{sp} is the specific capacitance, Is represents the current density, ΔT is the time of charge and discharge cycle, ΔV is the potential window, m is the mass of the active electrode material, E_g is the energy density in Wh/kg and P_g is the power density in W/kg. Table 5 showed the obtained values of all the supercapacitor devices assembled. All values of the energy density and power density lie in the region of the supercapacitor in a typical Ragone plot. However, like previous results, the 2% Mn-doped ZnO NW samples synthesized at 800 W showed the highest values of energy and power density. The overall better performance of the 2% Mn-doped sample can be attributed to firstly, its synthesis at 800 W power which gives dense nanowire morphology to provide more electrochemical sites for the reaction to take place as explained previously. While 2% doped Mn provides an optimum balance that extrinsic defect from Mn provides to the crystal structure of ZnO to enhance the supercapacitor performance without saturation and not over-straining the lattice. Zhang *et al*. showed that increasing defect centers after a certain limit will start to reduce the performance of supercapacitors [54]. Mn

doping to a certain point will increase the performance and then due to excess defect sites start affecting the conductivity of the device also reported previously [55]. Where reaching the maximum performance of supercapacitor at 2% Mn doping is also reported in previous work [55-57].

Table 5: Specific Energy and Specific Power values obtained from Galvanostatic charge-discharge at the current density of 0.15 A/g

Design	**Energy density Wh/kg**	**Power density W/kg**
1% Mn-doped ZnO NW 160W	0.72	1464.4
1% Mn-doped ZnO NW 800W	0.41	1470
1% Cu-doped ZnO NP 1	0.94	1464.9
2% Mn-doped ZnONW 160W	0.65	1490.4
2% Mn-doped ZnONW 800W	1.67	1495.5
2% Cu-doped ZnONP 1	0.27	1495.3
5% Mn-doped ZnO NW 160W	0.86	1481.3
5% Mn-doped ZnO NW 800W	0.94	1471.3
5% Cu-doped ZnO NP 1	0.48	1489.6

5. Conclusions

In conclusion, we have shown the synthesis of Mn and Cu doped ZnO, and using these samples as an electrode material provides a great opportunity to improve the performance of the supercapacitor device. To further enhance the performance of the supercapacitor, the metal-doped samples were used in combination with the synthesized MXene as the second electrode. The synthesized samples were analyzed in detail by various characterization techniques to get information on structural properties by XRD, electronic properties by Raman and EPR, optical analysis by PL, and electrochemical performance analysis through potentiostat. The primary importance in the analysis portion is given to the study of defect signals originating from the metal-doped ZnO as the performance of the supercapacitor depends heavily on these defects, and how we controlled these defect structures in metal oxides. EPR provided detailed information on the paramagnetic defect centers that originate when ZnO is doped with Mn and Cu and how the doping concentration affects these signals. The study also provides valuable information on how the morphology of the doped sample will have played its role in affecting the performance of the supercapacitor. The assembled supercapacitor showed value impressive values of energy density and power density, with the highest value

obtained for 800 W 2% Mn-doped ZnONW showing 1.67 Wh/kg energy density at a power density of 1495.5 W/kg. This study has provided some interesting research output that left room for further improvement in the area.

Conflicts of interest

There are no conflicts to declare.

Acknowledgments

This study is supported by a research grant from the Scientific and Technological Research Council of Turkey (TÜBITAK, Grant No: 118C243) in the frame of 2232-International Fellowship for Outstanding Researchers. The authors thank the Bio-nanotech Research and Innovation Tower (BRIT) laboratory of the University of Catania for the PHI Versa Probe XPS facility

References

1. Erdem, E., *Why P2X must be the part of the energy solution?* Environmental Progress & Sustainable Energy, 2021. **40**(3): p. e13545.
2. Wang, X., et al., *Flexible Energy-Storage Devices: Design Consideration and Recent Progress.* Advanced Materials, 2014. **26**(28): p. 4763-4782.
3. Guerrero, M.A., et al., *Supercapacitors: Alternative energy storage systems.* Przegląd Elektrotechniczny, 2009. **85**(10): p. 188-195.
4. Yildirim, I.D., et al., *Strategies to reach ultrahigh capacitance values for supercapacitors: materials design.* Turkish Journal of Physics, 2021. **45**(4): p. 178-184.
5. Wang, L., et al., *Preparation of Fe 3 O 4 with high specific surface area and improved capacitance as a supercapacitor.* Nanoscale, 2013. **5**(9): p. 3793-3799.
6. Najib, S. and E. Erdem, *Current progress achieved in novel materials for supercapacitor electrodes: mini review.* Nanoscale Advances, 2019. **1**(8): p. 2817-2827.
7. Zhang, X., et al., *Synthesis of porous NiO nanocrystals with controllable surface area and their application as supercapacitor electrodes.* Nano Research, 2010. **3**(9): p. 643-652.
8. Chen, S., et al., *Graphene oxide− MnO2 nanocomposites for supercapacitors.* ACS nano, 2010. **4**(5): p. 2822-2830.
9. Subramanian, V., et al., *Mesoporous anhydrous RuO2 as a supercapacitor electrode material.* Solid State Ionics, 2004. **175**(1-4): p. 511-515.
10. Ramadoss, A. and S.J. Kim, *Improved activity of a graphene–TiO2 hybrid electrode in an electrochemical supercapacitor.* Carbon, 2013. **63**: p. 434-445.
11. Dubal, D.P., et al., *Ultrathin Mesoporous RuCo2O4 Nanoflakes: An Advanced Electrode for High-Performance Asymmetric Supercapacitors.* ChemSusChem, 2017. **10**(8): p. 1771-1782.
12. Kim, C.H. and B.-H. Kim, *Zinc oxide/activated carbon nanofiber composites for high-performance supercapacitor electrodes.* Journal of Power Sources, 2015. **274**: p. 512-520.
13. Lee, K.S., C.W. Park, and J.-D. Kim, *Synthesis of ZnO/activated carbon with high surface area for supercapacitor electrodes.* Colloids and Surfaces A: Physicochemical and Engineering Aspects, 2018. **555**: p. 482-490.
14. Pant, B., et al., *Carbon nanofibers wrapped with zinc oxide nano-flakes as promising electrode material for supercapacitors.* Journal of Colloid and Interface Science, 2018. **522**: p. 40-47.
15. Najib, S., et al., *Tailoring morphology to control defect structures in ZnO electrodes for high-performance supercapacitor devices.* Nanoscale, 2020. **12**(30): p. 16162-16172.
16. Kaftelen, H., et al., *EPR and photoluminescence spectroscopy studies on the defect structure of ZnO nanocrystals.* Physical Review B, 2012. **86**(1): p. 014113.

17. Saleh, N.B., et al., *Importance of doping, dopant distribution, and defects on electronic band structure alteration of metal oxide nanoparticles: Implications for reactive oxygen species.* Science of The Total Environment, 2016. **568**: p. 926-932.
18. Fan, Z., et al., *Modified MXene/Holey Graphene Films for Advanced Supercapacitor Electrodes with Superior Energy Storage.* Advanced Science, 2018. **5**(10): p. 1800750.
19. Xia, Q.X., et al., *High volumetric energy density annealed-MXene-nickel oxide/MXene asymmetric supercapacitor.* RSC advances, 2017. **7**(18): p. 11000-11011.
20. Zhao, M.Q., et al., *Flexible MXene/carbon nanotube composite paper with high volumetric capacitance.* Advanced materials, 2015. **27**(2): p. 339-345.
21. Anasori, B., M.R. Lukatskaya, and Y. Gogotsi, *2D metal carbides and nitrides (MXenes) for energy storage.* Nature Reviews Materials, 2017. **2**(2): p. 16098.
22. Xu Zhang, Z.Z., Zhen Zhou, *MXene-based materials for electrochemical energy storage.* Journal of Energy Chemistry, 2018. **27**(1): p. 73-85.
23. Kumar, K.S., et al., *Recent advances in two-dimensional nanomaterials for supercapacitor electrode applications.* ACS Energy Letters, 2018. **3**(2): p. 482-495.
24. Ghidiu, M., et al., *Ion-exchange and cation solvation reactions in Ti3C2 MXene.* Chemistry of Materials, 2016. **28**(10): p. 3507-3514.
25. Sang, X., et al., *Atomic defects in monolayer titanium carbide (Ti3C2T x) MXene.* ACS nano, 2016. **10**(10): p. 9193-9200.
26. Ammar, A.U., et al., *ZnO and MXenes as electrode materials for supercapacitor devices.* Beilstein Journal of Nanotechnology, 2021. **12**: p. 49-57.
27. Liu, R., et al., *Fabrication of Cobaltosic Oxide Nanoparticle-Doped 3 D MXene/Graphene Hybrid Porous Aerogels for All-Solid-State Supercapacitors.* Chemistry – A European Journal, 2019. **25**(21): p. 5547-5554.
28. Zhang, M., et al., *Improving the performance of a titanium carbide MXene in supercapacitors by partial oxidation treatment.* Inorganic Chemistry Frontiers, 2020. **7**(5): p. 1205-1211.
29. Kannan, K., et al., *Fabrication of ZnO-Fe-MXene Based Nanocomposites for Efficient CO2 Reduction.* Catalysts, 2020. **10**(5): p. 549.
30. Wei, Y., et al., *All pseudocapacitive MXene-MnO2 flexible asymmetric supercapacitor.* Journal of Energy Storage, 2022. **45**: p. 103715.
31. Li, X., et al., *MXene (Ti3C2Tx) anodes for asymmetric supercapacitors with high active mass loading.* Materials Chemistry and Physics, 2021. **268**: p. 124748.
32. Yüksel Price, B., et al., *Effects of MnO doping on the electronic properties of zinc oxide: 406 GHz electron paramagnetic resonance spectroscopy and Newman superposition model analysis.* Journal of Applied Physics, 2015. **118**(17): p. 175705.
33. Thaweesaeng, N., et al., *Structure Properties of As-synthesized Cu-doped ZnO Nanopowder Synthesized by Co-precipitation Method.* Energy Procedia, 2013. **34**: p. 682-688.
34. Toloman, D., et al., *Evidence by EPR of ferromagnetic phase in Mn-doped ZnO nanoparticles annealed at different temperatures.* Journal of Alloys and Compounds, 2013. **551**: p. 502-507.
35. Mahmood, M., et al., *Synthesis of Ultrathin MnO2 Nanowire-Intercalated 2D-MXenes for High-Performance Hybrid Supercapacitors.* Energy & Fuels, 2021. **35**(4): p. 3469-3478.
36. Fang, H., et al., *Enhanced visible light photocatalytic activity of CdS with alkalized Ti3C2 nano-sheets as co-catalyst for degradation of rhodamine B.* Journal of Materials Science: Materials in Electronics, 2019. **30**(16): p. 14954-14966.
37. Tariq, A., et al., *Efficient Visible-Light Photocatalysis of 2D-MXene Nanohybrids with Gd3+- and Sn4+-Codoped Bismuth Ferrite.* ACS Omega, 2018. **3**(10): p. 13828-13836.
38. Aleinawi, M.H., et al., *Spectroscopic Probing Of Mn-Doped ZnO Nanowires Synthesized via a Microwave-Assisted Route.* The Journal of Physical Chemistry C, 2022. **126**(8): p. 4229-4240.
39. Presser, V., et al., *First-order Raman scattering of the MAX phases: Ti2AlN, Ti2AlC0.5N0.5, Ti2AlC, (Ti0.5V0.5)2AlC, V2AlC, Ti3AlC2, and Ti3GeC2.* Journal of Raman Spectroscopy, 2012. **43**(1): p. 168-172.
40. Iqbal, A. and N.M. Hamdan, *Investigation and Optimization of Mxene Functionalized Mesoporous Titania Films as Efficient Photoelectrodes.* Materials (Basel), 2021. **14**(21).

41. Sarycheva, A. and Y. Gogotsi, *Raman Spectroscopy Analysis of the Structure and Surface Chemistry of Ti3C2Tx MXene.* Chemistry of Materials, 2020. **32**(8): p. 3480-3488.
42. Spanier, J.E., et al., *Vibrational behavior of the ${M}_{n+1}A{X}_{n}$ phases from first-order Raman scattering $(M=\mathrm{Ti},\mathrm{V},\mathrm{Cr},$ $A=\mathrm{Si},$ $X=\mathrm{C},\mathrm{N})$.* Physical Review B, 2005. **71**(1): p. 012103.
43. Wang, Y., D.C. Alsmeyer, and R.L. McCreery, *Raman spectroscopy of carbon materials: structural basis of observed spectra.* Chemistry of Materials, 1990. **2**(5): p. 557-563.
44. Melchior, S.A., et al., *High-voltage symmetric supercapacitor based on 2D Titanium Carbide (MXene, Ti2CTx)/carbon nanosphere composites in a neutral aqueous electrolyte*. 2018.
45. Cao, Y., et al., *Enhanced thermal properties of poly(vinylidene fluoride) composites with ultrathin nanosheets of MXene.* RSC Advances, 2017. **7**(33): p. 20494-20501.
46. Wilhelmsson, O., et al., *Deposition and characterization of ternary thin films within the Ti–Al–C system by DC magnetron sputtering.* Journal of Crystal Growth, 2006. **291**(1): p. 290-300.
47. Myhra, S., J.A.A. Crossley, and M.W. Barsoum, *Crystal-chemistry of the Ti3AlC2 and Ti4AlN3 layered carbide/nitride phases—characterization by XPS.* Journal of Physics and Chemistry of Solids, 2001. **62**(4): p. 811-817.
48. Mashtalir, O., et al., *Intercalation and delamination of layered carbides and carbonitrides.* Nature Communications, 2013. **4**(1): p. 1716.
49. Jakes, P. and E. Erdem, *Finite size effects in ZnO nanoparticles: An electron paramagnetic resonance (EPR) analysis.* physica status solidi (RRL)–Rapid Research Letters, 2011. **5**(2): p. 56-58.
50. Li, X., et al., *Carbon and Graphene Quantum Dots for Optoelectronic and Energy Devices: A Review.* Advanced Functional Materials, 2015. **25**(31): p. 4929-4947.
51. Hong, L., R.F. Klie, and S. Öğüt, *First-principles study of size- and edge-dependent properties of MXene nanoribbons.* Physical Review B, 2016. **93**(11): p. 115412.
52. Al-Asadi, A.S., et al., *Aligned carbon nanotube/zinc oxide nanowire hybrids as high performance electrodes for supercapacitor applications.* Journal of Applied Physics, 2017. **121**(12): p. 124303.
53. Yang, Q., et al., *Rationally designed hierarchical MnO2-shell/ZnO-nanowire/carbon-fabric for high-performance supercapacitor electrodes.* Journal of Power Sources, 2014. **272**: p. 654-660.
54. Zhang, J., et al., *Remarkable supercapacitive performance of TiO2 nanotube arrays by introduction of oxygen vacancies.* Chemical Engineering Journal, 2017. **313**: p. 1071-1081.
55. Prashad Ojha, D., M. Babu Poudel, and H. Joo Kim, *Investigation of electrochemical performance of a high surface area mesoporous Mn doped TiO2 nanoparticle for a supercapacitor.* Materials Letters, 2020. **264**: p. 127363.
56. Patil, D., et al., *An Mn doped polyaniline electrode for electrochemical supercapacitor.* Journal of the Electrochemical Society, 2011. **158**(6): p. A653.
57. Phonsuksawang, P., et al., *Enhancing performance of NiCo2S4/Ni3S2 supercapacitor electrode by Mn doping.* Electrochimica Acta, 2021. **368**: p. 137634.